The Unpredictable Nature of Internal Tides on Continental Shelves

JONATHAN D. NASH

College of Earth, Ocean and Atmospheric Sciences, Oregon State University, Corvallis, Oregon

SAMUEL M. KELLY

University of Western Australia, Perth, Western Australia, Australia

EMILY L. SHROYER AND JAMES N. MOUM

College of Earth, Ocean and Atmospheric Sciences, Oregon State University, Corvallis, Oregon

TIMOTHY F. DUDA

Woods Hole Oceanographic Institution, Woods Hole, Massachusetts

(Manuscript received 6 February 2012, in final form 5 June 2012)

ABSTRACT

Packets of nonlinear internal waves (NLIWs) in a small area of the Mid-Atlantic Bight were 10 times more energetic during a local neap tide than during the preceding spring tide. This counterintuitive result cannot be explained if the waves are generated near the shelf break by the local barotropic tide since changes in shelfbreak stratification explain only a small fraction of the variability in barotropic to baroclinic conversion. Instead, this study suggests that the occurrence of strong NLIWs was caused by the shoaling of distantly generated internal tides with amplitudes that are uncorrelated with the local spring-neap cycle. An extensive set of moored observations show that NLIWs are correlated with the internal tide but uncorrelated with barotropic tide. Using harmonic analysis of a 40-day record, this study associates steady-phase motions at the shelf break with waves generated by the local barotropic tide and variable-phase motions with the shoaling of distantly generated internal tides. The dual sources of internal tide energy (local or remote) mean that shelf internal tides and NLIWs will be predictable with a local model only if the locally generated internal tides are significantly stronger than shoaling internal tides. Since the depth-integrated internal tide energy in the open ocean can greatly exceed that on the shelf, it is likely that shoaling internal tides control the energetics on shelves that are directly exposed to the open ocean.

1. Introduction

Some special coastal locations give rise to internal tides and nonlinear internal waves (NLIWs) that appear like clockwork, being phase-locked with individual flood/ebb events. In these locations, internal tide energetics track the surface forcing, with the largest internal waves occurring during spring tides. Such dynamics occur where 1) the geometry of the system is sufficiently constrained and wave generation localized in space, 2) tidal signals are significantly stronger than either the mesoscale or other broadband internal motions, and 3) there is a relatively quiescent waveguide through which signals propagate predictably. Semienclosed basins such as Massachusetts Bay (Scotti et al. 2008), the Bay of Biscay (Pingree and New 1991; Gerkema et al. 2004), and the South China Sea (Ramp et al. 2010; Li and Farmer 2011) represent some such examples.

Open-ocean wavefields close to strong generation sites like the Hawaiian Ridge also represent locations where internal tides are largely predictable from the surface forcing and background stratification (Lee et al. 2006; Carter et al. 2008; Colosi and Munk 2006; Zilberman et al. 2011). As a result, a significant fraction of the mode-1 internal tide variance may be described by time-invariant harmonic constants near major sites of generation (Dushaw et al. 2011).

Corresponding author address: Jonathan D. Nash, 104 CEOAS Admin. Bldg., Oregon State University, Corvallis, OR 97331.
E-mail: nash@coas.oregonstate.edu

DOI: 10.1175/JPO-D-12-028.1

In contrast, tidally generated internal wave energy that has radiated far from its origin may undergo propagation speed and path alteration via mesoscale variability (Rainville and Pinkel 2006). This tends to scramble the phase of wave arrivals, and may create complex temporal or spatial interference patterns (Rainville et al. 2010). As a result, propagating signals quickly become incoherent (Chavanne et al. 2010; Zilberman et al. 2011) so only a small fraction of the mode-1 variance can be described by harmonic analysis once the internal tide has traveled O(1000 km) from its source (Dushaw et al. 2011).

Similarly, internal tides on continental shelves and near coastal margins typically have significant low-frequency variability (MacKinnon and Gregg 2003; Lerczak et al. 2003; Sherwin et al. 2002; Savidge et al. 2007; Osborne et al. 2011). Much of this variability has historically been associated with changes in wind- and freshwater-driven mesoscale circulation, which alter the stratification, background currents and shear. As a result, propagation pathways and wave generation locations can be modified, especially if shelfbreak geometry is complex. Additionally, the internal tides can be Doppler shifted, leading to interference patterns that change on relatively short time scales. As a result, the occurrence and amplitude of NLIWs in such environments may not be connected to the strength of the tidal forcing. On the Malin Shelf, for example, larger NLIWs were observed during neap tides than spring (Small et al. 1999; Inall et al. 2000), indicating that the internal wavefield is not simply linked to the local forcing. Small et al. (1999) hypothesized that the energy for the NLIWs observed in that study may have originated from a distant source, with the solitons emerging from a shoaling internal tide as it reached shallower water.

Throughout this paper the term ''internal tide'' is used to describe internal waves generated by the tides but which span a broader frequency spectrum than the discrete frequencies of the astronomical forcing. We recognize that this is a broad definition, encompassing two classes of motions. The first are repeatable signals that can be described by a series of sinusoidal constituents at the astronomical frequencies. The second are motions with similar origins, yet which have been scattered, Doppler shifted or otherwise transformed into waves whose amplitudes and phases are modulated in time. Spectrally, this widens the bandwidth of the tidal line spectrum (Colosi and Munk 2006), which ultimately merges into the internal wave continuum. Here, we term all the above motions as internal tides and use the terms *coherent* and *incoherent* to distinguish between the constant- and variable-phase constituents that Colosi and Munk (2006) referred to as ''line'' and ''band.''

a. Waves on the New Jersey Shelf

The shelf east of New Jersey (NJ) is a region where NLIWs have routinely been observed. These have historically been thought to be generated by the action of barotropic tides over the continental slope, which is highly supercritical. However, most evidence of NLIW occurrence (i.e., amplitude, timing, etc.) stems from short time series (e.g., the shallow water acoustics experiment ''SWARM''; Apel et al. 1997), so there has been little ability to establish a link to the local forcing at the shelf break.

A detailed observational campaign was carried out in the summer of 2006 on the New Jersey continental shelf to study coastal dynamics, internal waves, acoustic propagation, and linkages between these [Office of Naval Research (ONR) Shallow Water 2006 (SW06) and NonLinear Internal Waves Initiative (NLIWI)]. Data were collected from 64 moorings deployed for 35–50 days, and from multiple ship operations that spanned from the shelf break to the central shelf, approximately 50 km inshore (Fig. 1).

One of the most noteworthy results from SW06/NLIWI was the finding that the largest and most energetic nonlinear internal waves occurred during the weakest barotropic forcing (Shroyer et al. 2010a). Wave displacements during spring tides ($\eta \approx 10$ m) were typically half of those during neap ($\eta \approx 20$ m; Shroyer et al. 2011), and carried approximately $^1/_{10}$ the energy and energy flux. These results are summarized in Fig. 1. Details of the energy flux calculations are presented in section 2. For reference, a 24.8-h hodogram of barotropic velocity at the shelf break (170-m isobath) from the middle of each time period is also shown, illustrating both the change in amplitude of the forcing and the relative contributions of diurnal and semidiurnal signals.

In this paper, data from five onshelf moorings spanning the 60–80-m isobaths are used to describe the low-frequency time evolution of NLIW field, and three moorings spanning the 120–470-m isobaths at the shelf break are used to describe the conditions at the hypothesized generation region. Our goal is to relate the cycle of NLIW energetics *on the shelf* to the dynamics *at the shelf break*. Shelfbreak conditions were also modeled using a 2D implementation of the nonhydrostatic MIT general circulation model for the purpose of deciphering the assorted signals present in the data.

b. Forcing mechanisms

Because NLIW packets were often observed inshore of the shelf break at this and other coastal sites (Apel et al. 1997, and others), their emergence was linked to the local barotropic tidal velocity u_{bt}, which heaves

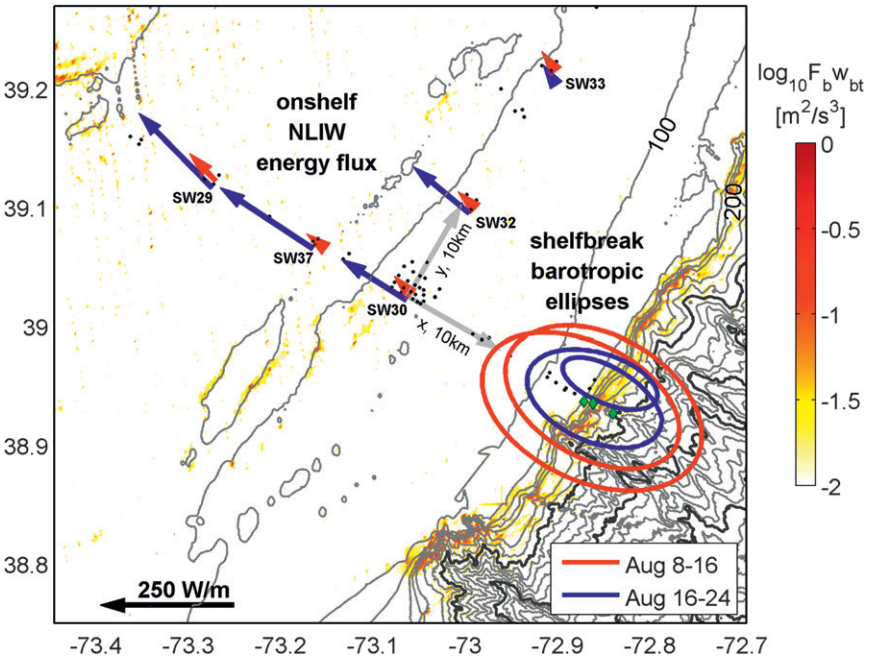

FIG. 1. Observational setting. Vectors represent the time-mean NLIW energy flux during spring (red; 8–16 Aug) and neap tides (blue; 16–24 Aug) at 5 onshelf moorings. Ellipses show a 25-h progression of depth mean current at the central shelfbreak mooring on 12 Aug (red; 10 cm s^{-1} max) and 20 Aug (blue; 6 cm s^{-1} max), roughly corresponding to spring and neap periods. Bathymetry is contoured at 25-m intervals at depths less than 200 m, and 100 m otherwise. Green diamonds indicate locations of the three shelfbreak moorings used in this analysis. Color shading represents the logarithm of Baines power [Eq. (2)], evaluated at $z = -H$ using observed N and the modeled M_2 tide from TPXO (Egbert 1997). We use a coordinate system rotated 30° clockwise from true north, with origin at SW30 as indicated by the light gray arrows, each 10 km long.

isopycnals at sloping topography, radiating internal tides (Rattray 1960; Baines 1982). The rate of energy conversion C from surface to internal tides appears in the energy equations as a sink for barotropic motions and a source for baroclinic ones (Kurapov et al. 2003; Kelly et al. 2010). It may be explicitly computed as the product of barotropic-induced vertical velocity $w_{\rm bt} = \nabla H \cdot \mathbf{u}_{\rm bt}$ and the internal tide pressure p' as

$$C = \nabla H \cdot \overline{\mathbf{u}_{\rm bt} p'}\big|_{z=-H}, \qquad (1)$$

where $\overline{()}|_{z=-H}$ represents a tidal average evaluated at the bottom, $z = -H$. Here, C may be evaluated from observations if full-depth velocity and density time series are available (Kelly et al. 2010; Kelly and Nash 2010; Zilberman et al. 2011).

A convenient diagnostic for C follows from Baines (1982), in which p' is approximated in terms of the Baines force $F_b = N^2 w_{\rm bt} \omega^{-1}$, where N and ω are the buoyancy and tidal frequencies, and $w_{\rm bt} = (z/H)\mathbf{u}_{\rm bt} \cdot \nabla H$ is taken to be the barotropically induced vertical velocity. This produces a vertical profile for the forcing

$$F_b w_{\rm bt} = \frac{N^2 (\mathbf{u}_{\rm bt} \cdot \nabla H)^2 (z/H)^2}{\omega}. \qquad (2)$$

While this formulation is not identical to C (i.e., the internal tide response is explicitly prescribed; see Duda and Rainville 2008, for details), it provides a convenient scaling that can be computed from barotropic tides, N^2 climatology, and bathymetry alone. On the New Jersey Shelf, $F_b w_{\rm bt}$ is broadly distributed along the 200-m isobath, with peaks near our moorings and near a canyon 20 km to the southwest (Fig. 1).

Based on the paradigm that NLIWs emerge from local forcing alone, the spring/neap cycle of tidal forcing combined with mesoscale changes in stratification would be sufficient to predict NLIW variability. However, as described anecdotally above and illustrated more quantitatively using rms vertical velocity as a metric (Figs. 2a,b), the low-frequency evolution of NLIW intensity correlates poorly with the spring/neap forcing (Figs. 2c,d). And while N^2 increased modestly during the experimental campaign (Fig. 2d), that change was insufficient to counteract the spring/neap cycle of $\mathbf{u}_{\rm bt}$ in $w_{\rm bt} F_b$ (Fig. 2e).

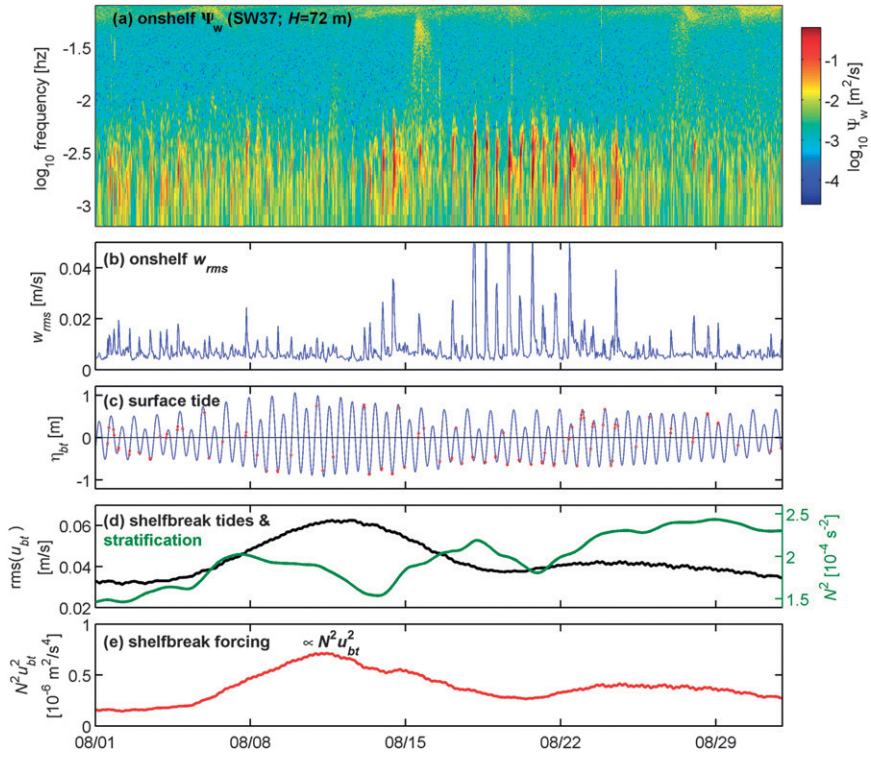

FIG. 2. (a) Spectrogram of midcolumn vertical velocity (mean over $24 < z < 50$ m depth) at midshelf mooring SW37; warm colors indicate the passage of NLIW packets. (b) NLIW occurrence is summarized using vertical velocity variance in the 100–1000-s wave band as a metric (rms w is plotted). (c) Surface tide elevation η_{bt}; red dots indicate arrival times of NLIW packets. (d) Cross-shelf barotropic tide u_{bt} (black) and stratification N^2 (green; computed as an average below $z = 25$ m) contribute to the locally generated internal tide at the shelf break. (e) $N^2 u_{bt}^2$ represents the time-varying contribution to the Baines forcing [Eq. (2)].

An alternate hypothesis to describe the time variability of shelf NLIWs (and internal tides) is the influence of pelagic internal tides (i.e., internal tides that are generated at distant locations) that shoal on the continental slope. It is our objective here to assess the relative contributions from shoaling and locally generated waves. First, we quantify internal tide and NLIW energies and relate these to the local barotropic tide and an estimate of the locally produced internal tide. A 2D numerical model is then used to strengthen our argument that changes in shelfbreak stratification can only weakly alter local generation. We then look more closely at the tidal energetics at the shelf break. By identifying phase-coherent and phase-incoherent motions, we provide an estimate of the locally generated internal tide, which scales with the strength of the barotropic tide but primarily exports its energy offshore. Conversely, internal tide energy flux associated with phase-incoherent motions is primarily directed onshore. Since its temporal structure is sufficiently different than the local spring/neap cycle of barotropic forcing, we associate these incoherent motions with the shoaling of a remotely-generated internal tide, whose phase has been scrambled by mesoscale effects.

2. Data and methods

Moorings were deployed over the New Jersey shelf and upper slope from approximately 28 July to 12 September 2006. Details of the instruments and their locations are given in Shroyer et al. (2011) and Newhall et al. (2007). We use five moorings (SW 29, 30, 32, 33, 37) with nearly full-depth ADCP and sparsely sampled CTD (3–11 sensors per mooring) to evaluate the on-shelf energetics. Three shelfbreak moorings that spanned the 125–470-m isobaths (SW 34/40 pair, 42 and 43) had good vertical CTD and ADCP coverage (e.g., SW43 had 27 T or C/T sensors and 2 ADCPs) and were used to describe shelfbreak dynamics. High vertical resolution shipboard surveys (Shroyer et al. 2011) and glider transects (Castelao et al. 2008) are used to augment the on-shelf moored data in order to define the background stratification.

The energy transport in NLIWs is quantified following the methods described in Scotti et al. (2006), Moum et al. (2007), and Lamb (2007). In the following we quantify the NLIW energy flux density F_E^*, which is composed of three terms:

$$F_E^* = u'(p' + E_k + E_a). \tag{3}$$

The first term represents the correlation between wave velocity u' and pressure p', which dominates in the linear limit of small waves (Brickman and Loder 1993; Nash et al. 2005). The advection of kinetic energy (KE) density, $E_k = \rho(u'^2 + v'^2)/2$, and the advection of available potential energy (APE) density E_a can contribute significantly. The calculation of these terms is explained in the appendix.

For semidiurnal internal tides, the energy flux is adequately approximated by the linear, hydrostatic contribution:

$$F_E = u'p', \tag{4}$$

where $p' = p'_h + p'_\eta$, with the free-surface pressure p'_η estimated by requiring $\int_{-H}^{0} p'\,dz = 0$ (Nash et al. 2005). For this purpose, in situ densities and ADCP-derived velocities were bandpass filtered to retain 3–48-h variability. Fluxes were estimated using either the raw bandpassed time series or from time series regenerated from multifrequency harmonic analysis (more details are provided in section 4e).

3. On-shelf NLIWs

a. Identification and quantification

As illustrated in Fig. 2, vertical velocity is a useful metric for identifying NLIWs. To quantify F_E^*, start and stop times of every potential wave event were subjectively identified using a manual screening of ADCP records. The coordinate rotation that minimizes cross-wave velocity variance was applied to yield u' in a reference frame aligned with the propagation direction x, which was typically 30°S of E (i.e., waves propagate in the $-x$ direction; see Shroyer et al. 2011 for a distribution of wave propagation directions). The streamfunction was then computed to determine wave displacements. To remove contamination from the vertical advection of background shear, the background velocity profile was subtracted along streamlines (as opposed to simply removing the velocity as a function of depth). Vertical velocity was assumed to be entirely associated with the waves, $w = w'$. From these were derived the wave-induced streamfunction ψ, which was combined with a ship- or glider-derived ρ_o to determine ρ', p', E_a and E_k.

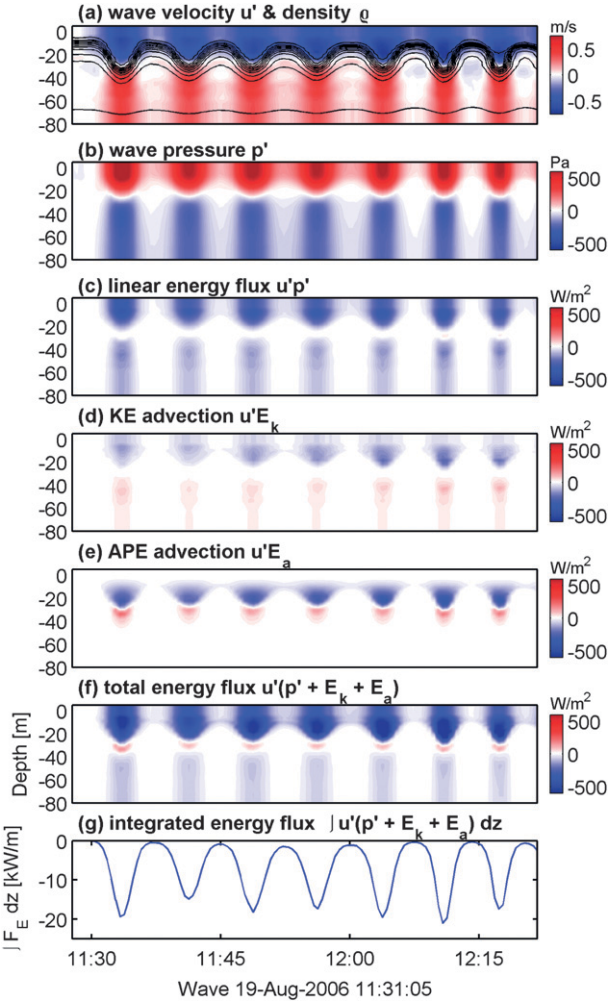

FIG. 3. Contributions to the energy flux, as calculated at the central mooring (SW30) for a relatively large wave packet on 19 Aug 2006. This disturbance lasted almost 4 h and consisted of more than 30 waves; only the first 7 are presented here. Shown are the time/space evolution of (a) wave velocity u' and total density ρ, (b) wave pressure p', (c) linear contribution to the energy flux $u'p'$, (d) advection of KE, (e) advection of APE, and (f) total energy flux F_E^*. The vertical integral of (f) is shown in (g). All quantities have been rotated so that the wave is propagating in the $-x$ direction (blue represents onshore velocity and energy flux/advection).

The various contributions to F_E^* for a typical large wave during neap tides are illustrated in Fig. 3. The nonlinearity of these wave packets is immediately apparent from u' (Fig. 3a), which has a time-average velocity profile that is onshore above the pycnocline, and offshore below it, leading to net onshore transport (Shroyer et al. 2010b). This contrasts a linear wave, for which the time-average u' and transport is zero.

Wave pressure is predominantly mode 1, (Fig. 3b) and anticorrelated with u', producing $u'p'$ (Fig. 3c) aligned with the propagation direction. As with u', p' does not

oscillate about 0, but is instead always positive/negative in the upper/lower part of the water column. Energy (and flux) computed by requiring time-average u' and p' to be zero (i.e., as in a linear wave Nash et al. 2005) would be significantly less, highlighting the waves' nonlinear nature. In addition, the waves often ride on top of a bore, which is associated with a net downward internal displacement (upward deflection of surface η) that spans the entire duration of the wave-packet and contributes to nonzero time average p'. This example thus serves to illustrate how linear wave assumptions are inappropriate for highly nonlinear waves with bore-like energy contributions, as proper identification of the reference state has important consequences (Henyey and Hoering 1997).

The advection of kinetic and available potential energy are shown in Figs. 3d,e. These are smaller than the contribution from $u'p'$ and typically represent about 40% or less of F_E^* (Moum et al. 2007). Importantly, $u'(E_k + E_a)$ has a different depth structure than $u'p'$ and opposes the direction of wave propagation in the lower part of the water column. Thus, while energy advection acts to enhance the near-surface F_E^*, it opposes it at depth. The total flux (Fig. 3f) and its depth-integral (Fig. 3g) are thus dominated by the near-surface contributions.

b. Temporal variability of F_E^*

A total of 349 NLIW packets were identified in the five on-shelf ADCP mooring records (~100 per mooring). For each event, the instantaneous energy flux was computed and integrated over depth and time, yielding the total onshore energy transport per wave event $E_{\text{tot}} = \int_{t_1}^{t_2} F_E^* \, dt$. Plotted on a logarithmic scale in Fig. 4a is the contribution of each NLIW event to the 24-h average $F_{E,24\text{h}}^* = E_{\text{tot}}/(24\,\text{h})$ along with the daily-averaged energy flux $\langle F_E^* \rangle_{24\text{h}}$, represented as a mean over all five moorings (the sum of $F_{E,24\text{h}}^*$ in each 24-h period, divided by 5; Fig. 4a, solid line). Plotting the same $\langle F_E^* \rangle_{24\text{h}}$ data on a linear scale (Fig. 4b) emphasizes the 16–24 August period of intense NLIW activity, when $\langle F_E^* \rangle_{24\text{h}}$ was elevated by more than a factor of 10.

This perspective also illustrates how the daily-averaged NLIW energy transport is dominated by a small number of strong wave packets, with most of the events being a factor of 10 weaker than those that contribute substantially to the mean. In addition, the largest energy transports often occur at the innermost mooring (blue squares; SW29). This is consistent with shipboard wave-tracking experiments (Shroyer et al. 2010a), which establish the approximate boundary between wave growth and wave decay (i.e., the location of peak NLIW energy) near SW29 ($x = -20$ km in Shroyer et al. 2010a). We also note that energy flux derived from shipboard wave tracking as cE (see Fig. 5 in Shroyer et al. 2010a) are statistically consistent with those presented here.

For comparison, the linear contribution to the internal tide energy flux [F_E from Eq. (4)] at the central shelf SW30 (blue line in Fig. 4b) was computed using band-passed u' and p'. The internal tide F_E and NLIW F_E^* have similar magnitude and temporal evolution, suggesting they may have the same energy source. Note, however, that F_E^* and F_E are not independent since NLIW velocity and pressure both project into the 3–48 h band we associate with internal tide motions.

In summary, NLIW and internal tide energy flux (F_E^* and F_E) covary and do so in a way that is out of phase with the local tidal forcing, as represented by $N^2 u_{\text{bt}}^2$ (Fig. 4c), a proxy reflecting the temporal changes in shelf-break generation. We highlight two periods in the record: 1) the period of strong tidal forcing and weak F_E^*, shaded pink in Fig. 4 and labeled *spring*, and 2) the period of strong NLIW activity, but weak tidal forcing, shaded blue in Fig. 4 and labeled *neap*.

4. Relating NLIW occurrence to shelfbreak dynamics

While the common evolution of NLIW and internal tide is expected (Lamb 1994; Colosi et al. 2001), the lack of correspondence between internal waves and barotropic tidal forcing was unexpected. To understand the observed disconnect between the local barotropic tidal forcing and occurrence of nonlinear internal waves on the shelf, we now explore the energy sources and dynamics that control the energetics of the internal tide.

a. Shelfbreak generation: Total conversion and effect of N^2

Numerical simulations were conducted to determine the magnitude of the expected local internal tide generation and the effect of stratification on net conversion C. The nonhydrostatic Massachusetts Institute of Technology (MIT) general circulation model (Marshall et al. 1997) was used in a 2D configuration representing the main mooring line [i.e., connecting shelf break (SW40–43) to onshelf moorings (SW29–30)]. The model was run in an 800-km long domain, with horizontal resolution of 250 m over the shelf and slope (telescoping to 2000 m offshore) and vertical resolution of 5 m above 200 m (telescoping to 30 m at depth); bathymetry was smoothed at 1-km resolution. Here, M_2 barotropic velocity forcing ($T = 12.42$ h) was applied at the offshore boundary to produce 0.1 m s^{-1} cross-shelf barotropic tides at the midshelfbreak mooring (SW42), consistent with those observed during spring tides (Fig. 1; red ellipses). Vertical and horizontal eddy viscosities of 10^{-3}

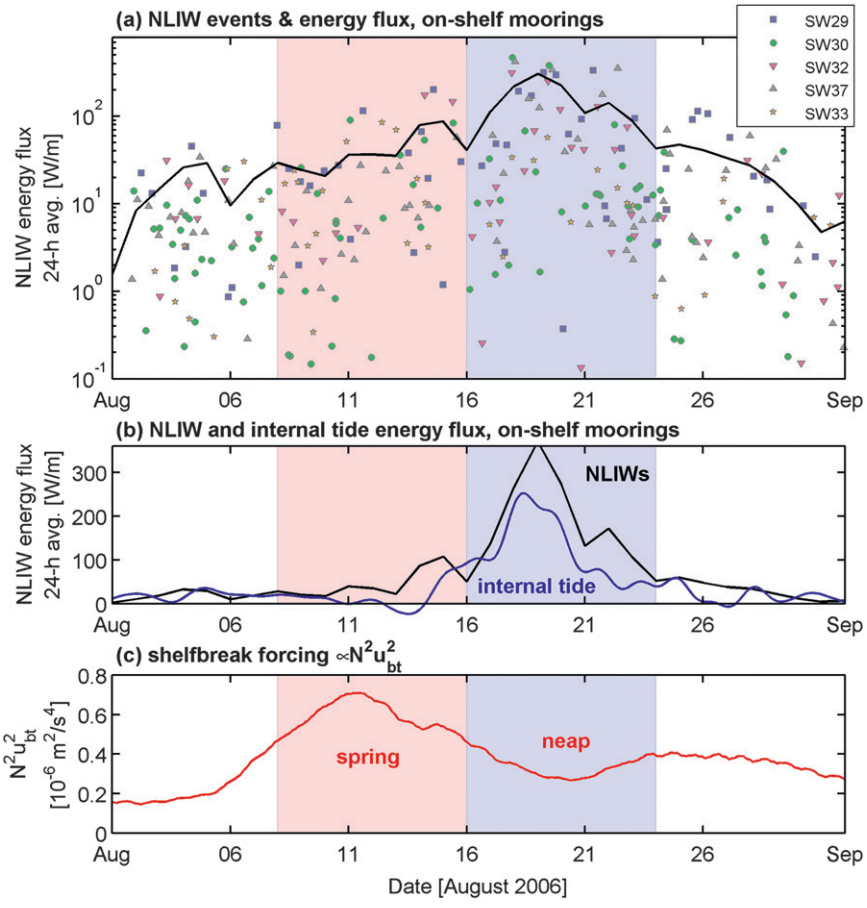

FIG. 4. NLIW intensity as a function of time. (a) Symbols represent the contribution from each NLIW packet to the daily-averaged energy flux $F^*_{E,24h}$, on a logarithmic scale. The black line represents the mean onshore energy transport, averaged over all five onshelf moorings, $\langle F^*_E \rangle_{24h}$. (b) $\langle F^*_E \rangle_{24h}$ plotted on a linear scale, along with the internal tide F_E at the central onshelf mooring. (c) Proxy for shelfbreak forcing, as in Fig. 2e. Note that all energy fluxes are depth integrals.

and 10^2 m^2 s^{-1} provided numerical stability and a flow relaxation scheme at the offshore boundary prevented spurious internal wave reflections into the domain. The model was sampled after the 10th tidal cycle.

To test the sensitivity of C to changes in N^2, simulations were run with two different vertical profiles of density, one corresponding to the period of weak NLIWs (8–16 August; blue in Fig. 5b) and one corresponding to the period of stronger NLIWs (16–24 August; green in Fig. 5b), during which the shelfbreak N^2 was approximately 25% stronger (see Fig. 2d).

Figure 5 shows the modeled energy flux $F_E = u'p'$ and its depth average for these two periods. Locations of the three shelfbreak moorings are identified; for reference, SW30 is located at $x = 0$ km. Several important attributes of this system are revealed through these simulations.

- Most of the barotropic loss at the shelf break is associated with internal tides that radiate *offshore*, not *onshore* toward the shelf. This is because the shelf break is strongly supercritical (characteristics are shown in black in Figs. 5c,d), so most locally-generated energy is radiated to the open ocean.
- The energy transmitted onshore is relatively weak. Based on these simulations, only ~10% of the converted energy (i.e., $\int C\,dx$) is transmitted onshore, amounting to a maximum of 20–40 W m^{-1} of $\int F_E\,dz$ at the 100 m isobath. This is small compared to the peak of 250 W m^{-1} observed at the onshelf moorings during neap tides (Fig. 4b).
- Total conversion $\int C\,dx$ scales roughly with N^2. However, the energy transmitted onto the shelf depends on the distribution of C and the shape of internal tide characteristics, which controls *where* the converted energy goes. Thus if stratification is weakened at depth, yet strengthened at the surface (as we observed following 16 August), a larger fraction of the converted

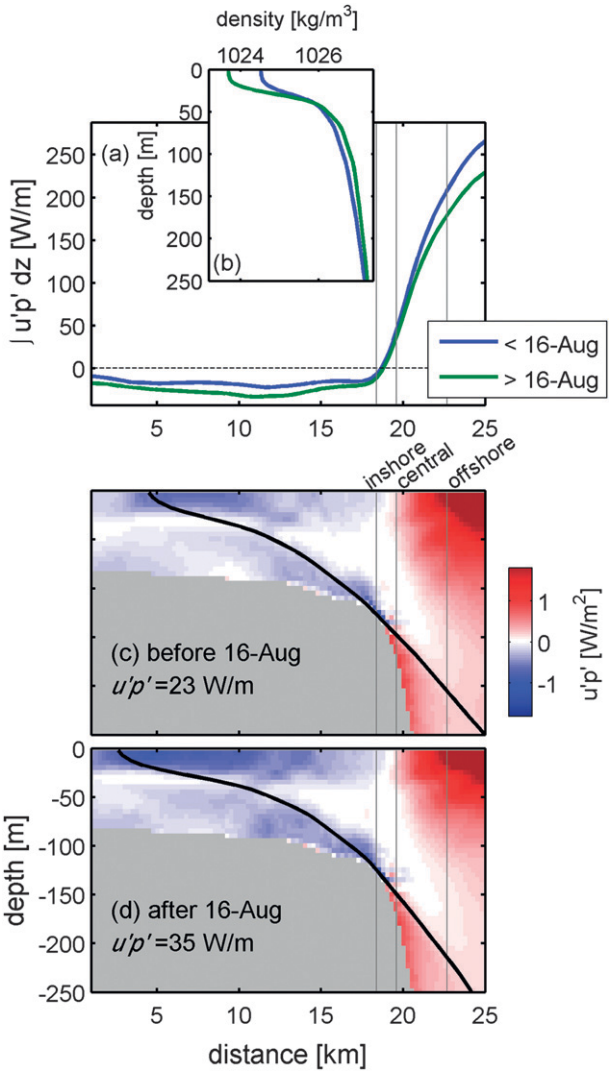

FIG. 5. Output of a barotropic-forced 2D model. (a) Depth-integrated baroclinic energy flux for the two different stratifications shown in (b). (c),(d) Spatial structure of the energy flux is shown. The model indicates that the critical slope is the approximate dividing location between net offshore and onshore energy flux. Generation over the slope mostly radiates offshore; the onshore component at $x = 10$ km is small and changes from 23 to 35 W m^{-1} depending on the stratification [indicated in (c) and (d)].

energy may be transmitted onshelf. For the two density profiles shown in Fig. 5b, a 25% increase in N^2 produces an approximate 50% *increase* in onshore energy flux, yet produces a *reduction* in offshore-transmitted internal tide energy.

- The inshore and central shelfbreak moorings (indicated with gray vertical lines in Figs. 5c,d) are in a region of minimum F_E, while the offshore mooring is at a location where modest offshore F_E should be observed.

In summary, for realistic spring-tide forcing across a 2D shelf and slope, predicted $\int F_E\, dz$ on the shelf is 20–40 W m^{-1}. This locally generated component is almost an order of magnitude smaller than those observed during the *neap* period of peak on-shelf F_E^* and F_E (Fig. 4b). While the model simulations indicate that enhanced N^2 during the *neap* period increases F_E by ~50% (or ~12 W m^{-1}) on the shelf, this is small compared to the factor of 10 increase observed (to ~200 W m^{-1}). Moreover, tidal forcing is reduced by 30%–50% during the neap period (Fig. 1; blue versus red ellipses), which nullifies the gain associated with N^2.

b. 3D effects and other sources of variability

Three-dimensional effects associated with variability in topography, stratification, or forcing can strongly influence the geographic distribution of C and the spatial structure of the propagating internal tide. Over the deep OR continental slope, Kelly et al. (2012) find significant internal tide generation from along-slope currents interacting with along-slope topographic variations, leading to strong gradients in F_E over the 10-km scales that characterize the underlying topographic variability. In semienclosed basins, the refraction, reflection, and scattering of internal tide energy can work to create resonances or basin-scale modes (e.g., Buijsman et al. 2012) that alter the resultant wavefield (Guo et al. 2011).

On continental shelves exposed to the open ocean, 3D effects can be important in shaping the internal tide's structure and energy. On the Portuguese shelf, for example, large-amplitude internal tides are believed to result from the interaction of local processes with those that originate 50 km farther along the slope (Sherwin et al. 2002), which are refracted by the 3D waveguide. Numerical modeling of the internal tide on the OR shelf (Osborne et al. 2011) indicate hotspots of generation and interference patterns that produce factor of 10 variability in C and F_E over relatively short spatial scales (10–100 km). While 3D internal-tide models have not yet been applied to the NJ shelf, it is likely that similar processes could be at play here. Evidence for three dimensionality comes from the strong along-shelf gradient in F_E^* (cf. the flux vectors at SW32 and SW33 in Fig. 1), which can frequently vary by a factor of 5 over 15–25 km. In addition, satellite imagery (e.g., Tang et al. 2007) often shows NLIW packets propagating in a variety of directions, suggestive of multiple generation regions.

In this paper we do not explore the consequences of three dimensionality to the structure of the energy flux (e.g., focusing and refraction), as we do not have the necessary measurements to do so. However, given the extremely low values of F_E predicted by the 2D model

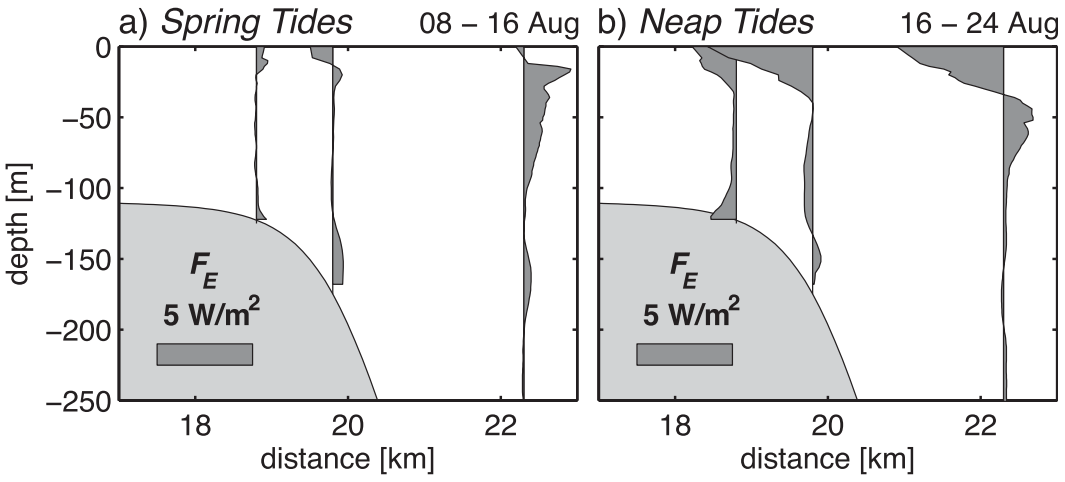

FIG. 6. Spatial structure of the total cross-shelf energy flux F_E during (a) spring and (b) neap periods.

and recognizing that even in a fully 3D model, we anticipate that C will scale with the spring-neap cycle, it seems likely that local generation cannot support the observed temporal evolution of on-shelf internal tides.

c. Dissipation at the shelf break

Weaker internal tides during the spring period could in theory be related to the amount of dissipation that occurs in the near-field region of generation sites. For example, if the forcing is strong enough, lee waves can be arrested at the generation site (e.g., Klymak et al. 2010a), increasing dissipation, and reducing the fraction of radiated energy. However, unlike a strongly forced, confined channel, Froude numbers at the shelf break (defined as the ratio of fluid velocity to the linear internal wavespeed c_n for mode n) are subcritical for the low modes. For example, at the 120-m isobath, the value of c_n for modes 1–3 is 0.75, 0.35, and 0.24 m s^{-1}. In comparison, neither barotropic nor near-bottom velocities exceed 0.25 m s^{-1} at that location, so low-mode Froude numbers are subcritical and most of the locally generated energy will be radiated, not dissipated (Klymak et al. 2010b). Furthermore, even if strong dissipation did occur for spring tides, there is insufficient energy propagating onshelf during neaps, leading us to search for an alternate source for the onshelf internal tides and NLIWs.

d. Structure of shelfbreak F_E

As illustrated in Fig. 6, the across-shelf energy flux at the shelf break has significantly different structure during spring and neap periods. During the spring period, F_E at the offshore mooring was modest and directed offshore, while F_E at the central and inner shelfbreak moorings was weak and with variable direction. This structure of F_E is qualitatively consistent with a wavefield dominated by locally-generated internal tide at the shelf break, (i.e., as modeled; Fig. 5).

During the neap period, F_E is predominantly shoreward at all 3 moorings, which is inconsistent with a wavefield driven by local generation. Only at the offshore mooring is there an offshore component to F_E, and this occurs only at depths greater than 50 m. During this time period, F_E appears to be dominated by a source offshore of the mooring array. We hypothesize that spatial distribution of F_E represents a superposition of a shoaling, remotely generated internal tide, with one that is locally generated on this slope. In the following section, we decompose the wavefield into phase-coherent and phase-incoherent motions with the goal of partitioning the energetics associated with locally and remotely generated internal tides.

e. Partitioning F_E associated with shoaling and shelfbreak-generated waves

In an attempt to decompose the shelfbreak internal wavefield into contributions associated with (i) locally generated internal tides, and (ii) shoaling, remotely generated internal tides, we assume that all motions that maintain a constant phase relationship at the astronomical tidal frequencies over the 40-day observational period are associated with local conversion from the barotropic tide. All other motions (those that do not maintain a constant phase relationship, but instead wander from day to day) we associate with conversion from the barotropic tide at some distant location, and may be associated with a shoaling tide.

We recognize that this decomposition will not completely isolate local and remote wavefields. Mesoscale variability in currents and stratification will modulate local generation (e.g., Hosegood and van Haren 2006),

and conversely, shoaling internal tides may also exhibit some degree of phase coherence depending on details of their origination and propagation. Moreover, if the locally-generated internal tide arises from 3D interactions that span 10–100 km along the slope (Sherwin et al. 2002 e.g.,), then those contributions may be attributed to the shoaling signal if their phase wanders (which is likely, at least to some extent). Nevertheless, we attempt the above decomposition because 1) the flux at the shelf break (Fig. 6) opposes the spring/neap cycle, and 2) time series of F_E on the shelf (Fig. 4b) is highly variable in time. For these data, this technique appears to successfully divide the wavefield in an informative way.

Contributions to u, v, and perturbation ρ' that are phase locked to the surface tides are extracted in the following way. First, data are bandpass-filtered to retain 3–48-h variability. Then, a 10-component harmonic fit is performed at each depth using a least squares minimization. We fit to $M_2, S_2, N_2, K_2, K_1, O_1, P_1, M_4, S_4$, and f to assign as much of the variance as possible to the coherent signal (i.e., tidal harmonics are assigned to the coherent signal if they are phase-locked). Finally, time series are regenerated from the harmonic fits and considered the coherent signal, while the residual is considered phase-incoherent:

$$u = u_{\text{coh}} + u_{\text{inc}}, \quad \rho' = \rho'_{\text{coh}} + \rho'_{\text{inc}}. \tag{5}$$

To calculate the energy flux, each of the coherent and incoherent variables are considered separately to compute perturbation velocity and pressure signals. For example, the coherent barotropic velocity is calculated as

$$(u_{\text{coh}})_{\text{bt}} = \int_{-H}^{0} u_{\text{coh}}\, dz, \tag{6}$$

the coherent baroclinic velocity as

$$u'_{\text{coh}} = u_{\text{coh}} - (u_{\text{coh}})_{\text{bt}} \tag{7}$$

and the coherent baroclinic pressure as

$$p'_{\text{coh}}(z) = g\int_{z}^{0} \rho'_{\text{coh}}\, dz' + (p_{\text{coh}})_o, \tag{8}$$

where $(p_{\text{coh}})_o = -\int_{-H}^{0} p'_{\text{coh}}\, dz$ is the surface pressure required to satisfy the baroclinicity condition (Kunze et al. 2002). Identical procedures as in Eqs. (6), (7), and (8) are applied to determine the incoherent perturbation velocity u'_{inc} and pressure p'_{inc}.

In the following, we assume $p'_{\text{nh}} \ll p'$ and $uE \ll u'p'$ in tidal-frequency waves (see the appendix for definitions), and decompose the linear contribution to F_E into its coherent and incoherent parts:[1]

$$\begin{aligned} F_E &= u'_{\text{coh}}p'_{\text{coh}} && \text{(coherent flux)}\\ &\quad + u'_{\text{coh}}p'_{\text{inc}} + u'_{\text{inc}}p'_{\text{coh}} && \text{(cross terms)}\\ &\quad + u'_{\text{inc}}p'_{\text{inc}} && \text{(incoherent flux)}\\ &= F_{\text{coh}} + F_{\text{cross}} + F_{\text{inc}}. \end{aligned} \tag{9}$$

The first and last terms result from purely phase-coherent or phase-incoherent motions and may be individually expected to be associated with one type of wave process or the other. As such, we anticipate these terms to be relatively well-behaved (spatially and/or temporally), especially F_{coh}. The cross terms (F_{cross}) represent energy transports associated with time-varying interference patterns of superimposed waves. Since there is no preferred phasing between coherent and incoherent motions (by construction), we anticipate the sign of the cross terms to be somewhat chaotic and largely unrelated to the dynamics of its constituent signals. For example, it is equally probable for F_{cross} to be positive or negative depending on how the waves interfere; its magnitude, however, is expected to scale with the product of the constituent signals.

f. Coherent and incoherent time series

Coherent and incoherent contributions to F_E were computed at the three shelfbreak moorings (inshore, SW40/SW34; central, SW42; and offshore, SW43). The decomposition produced similar results at each mooring, so a time evolution of its vertical structure is presented in detail only for SW43 (x = 22.3 km, H = 470 m depth) in Fig. 7; a summary of depth-averaged coherent and incoherent fluxes for all shelfbreak moorings is presented in Fig. 8.

The shelfbreak internal tide exhibits a complex structure characterized by 2–5-day bursts of energy distributed at various depths throughout the water column (Fig. 7b). $\int F_E\, dz$ is predominantly positive (Fig. 7a), consistent with offshore radiation of a shelfbreak-generated internal tide of magnitude 100–500 W m^{-1} (Figs. 5 and 6a). An exception is the several-day period surrounding 19 August, during which there is a burst of net energy onshelf.

Harmonic analysis (Figs. 7c,d) extracts the part of the internal tide that remains phase locked over a 40-day

[1] Note that retaining the nonlinear contributions complicates the decomposition because there are 10 cross terms in the triple products associated with uE_K and uE_a, even if E_a is linearized and approximated as $N^2\xi^2/2$.

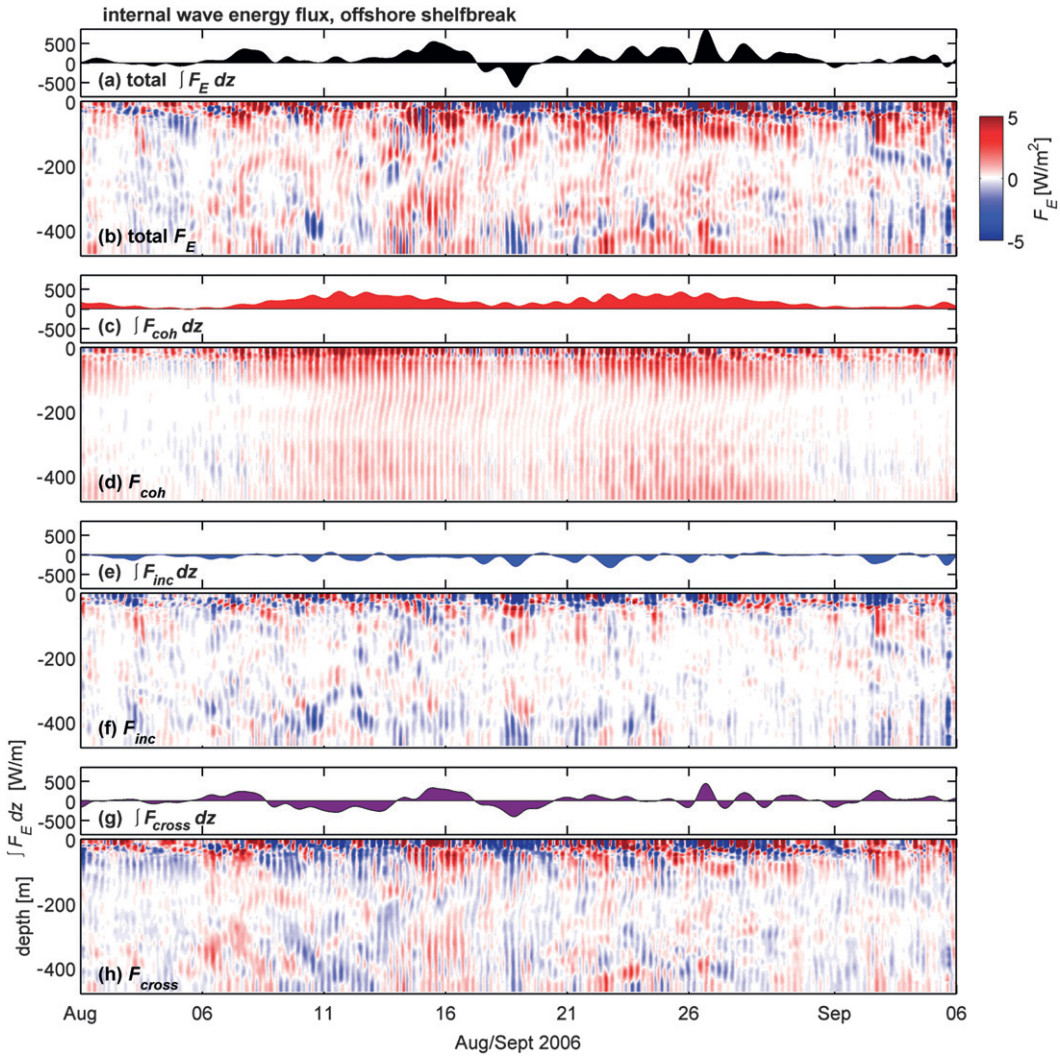

FIG. 7. Depth integrals and vertical structure of the energy flux at the farthest offshore mooring, SW43 (470-m depth). Shown is (a),(b) the total flux F_E, (c),(d) the coherent contribution F_{coh}, (e),(f) the incoherent contribution F_{inc}, and (g),(h) the contribution from the cross terms F_{cross}. Note that red is offshore and blue is onshore energy flux.

period (F_{coh}). While the total F_E is directed both on- and offshore, F_{coh} is predominantly positive and temporally follows the cycle of barotropic tidal forcing (Fig. 2), with maximum $\int F_{\mathrm{coh}}\,dz \approx 500\ \mathrm{W\,m^{-1}}$ during spring tides, $\int F_{\mathrm{coh}}\,dz < 100\ \mathrm{W\,m^{-1}}$ during neap, and time mean near 200 W m^{-1}, consistent with the 2D numerical simulations of local generation at $x = 22.3$ km (Fig. 5a).

In contrast to $\int F_{\mathrm{coh}}\,dz$, $\int F_{\mathrm{inc}}\,dz$ is almost exclusively negative and bursty, capturing variability without significant phase coherence (Figs. 7e,f). Because F_{inc} is predominantly directed onshore, these waves must have originated offshore or elsewhere on the slope, and have subsequently propagated onshore to this site. F_{inc} also has a more complex vertical structure than F_{coh}. Since high wavenumber internal waves travel more slowly than low wavenumbers, their travel times are more easily altered by Doppler shifting due to wave–wave or wave–current interactions. Hence, they are more likely to lose phase coherence and be associated with F_{inc}, even if their origin is nearby.

While F_{coh} and F_{inc} have simple physical interpretations and preferred orientations ($F_{\mathrm{coh}} \rightarrow$ offshore, $F_{\mathrm{inc}} \rightarrow$ onshore), the cross terms have no net preferred orientation (Figs. 7g,h). Instead, F_{cross} is associated with 2–5-day bursts of energy that alternate in sign depending on how u'_{coh} and p'_{inc} or u'_{inc} and p'_{coh} are phased. Because F_{cross} instantaneously has a magnitude similar to F_{coh} or F_{inc}, it can drastically alter the total flux F_E. The incoherent tide thus plays a dominant role in controlling how the total energy flux evolves, because it produces

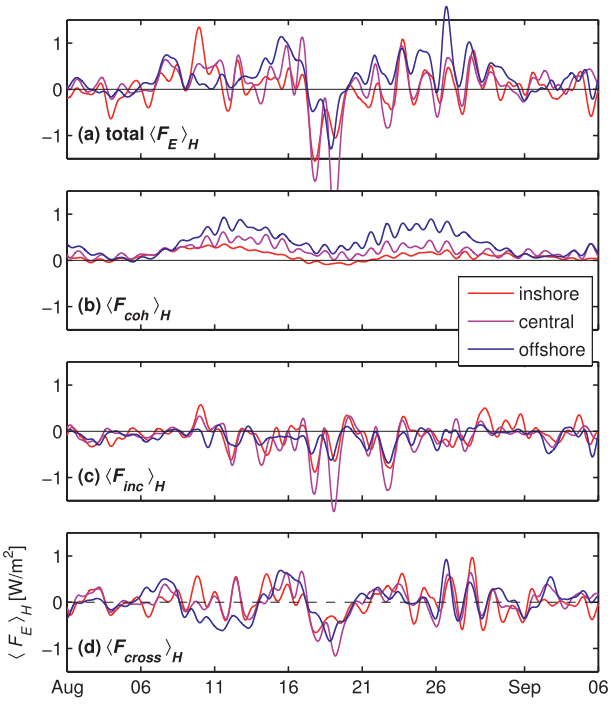

FIG. 8. Depth-averaged energy flux at offshore (470 m; blue), central (170 m; magenta) and inner (130 m; red) shelfbreak moorings. Shown is (a) the total flux F_E, (b) the coherent contribution F_{coh}, (c) the incoherent contribution F_{inc}, and (d) the contribution from the cross terms F_{cross}. Data are the same as in Fig. 7a,c,e,g, except depth averages are used instead of depth integrals to aid the comparison of data from moorings at different depths.

stochastic variability through contributions from both F_{inc} and F_{cross}.

The above decomposition appears to be an effective means of distinguishing contributions associated with 1) the seaward radiation of locally-generated internal tides, characterized through F_{coh}, and 2) the shoreward shoaling of internal tides generated remotely, characterized through F_{inc}. We highlight, however, that the total instantaneous F_E is not simply the sum of F_{coh} and F_{inc}, but includes important contributions from F_{cross} that can either enhance or reduce the F_E depending on the precise phasing between shoaling and locally-generated waves. Because F_{cross} has similar magnitude to the other terms, it can produce O(1) changes in F_E over short (1–3 day) time scales.

The time evolution of F_E at all shelfbreak moorings is summarized using depth averages (denoted by $\langle \cdots \rangle_H$) in Fig. 8. Qualitatively, $\langle F_E \rangle_H$ has similar temporal character at all shelfbreak moorings, characterized by 2–5-day variability, and punctuated by a burst of onshore-directed energy during the period surrounding day 19 (Fig. 8a).

The coherent/incoherent decomposition elucidates a number of cross-shelfbreak trends. First, $\langle F_{\text{coh}} \rangle_H$ extracts a similar spring/neap cycle of offshore-directed energy flux at all 3 moorings (Fig. 8b). In addition, $\langle F_{\text{coh}} \rangle_H$ increases by more than a factor of 3–5 moving offshore from the 130- to 470-m isobath, confirming that the slope is the source of internal tide energy that remains coherent over the 40-day period. Note that depth integrals (not shown) increase 10 × across the same region owing to the increasing depth.

On the other hand, $\langle F_{\text{inc}} \rangle_H$, is directed onshore and tends to be strongest at the central mooring (Fig. 8c). The temporal modulation of $\langle F_{\text{inc}} \rangle_H$ is not related to the spring-neap cycle but instead has variability that tracks the total flux $\langle F_E \rangle_H$. Notable in particular are 3 pulses of incoherent energy directed onshore between 17 and 23 August, which occur during the period of weak $\langle F_{\text{coh}} \rangle_H$. We have no reason to believe that the timing of these pulses has any unique relationship to the local spring/neap cycle. Depth integrals of F_{inc} decrease from offshore to inshore moorings, suggesting that some fraction of this incoming wavefield is dissipated on the slope. Note that a substantial fraction of the incoming energy is still transmitted to the shelfbreak. We also expect some fraction of a shoaling internal tide to be radiated back to the open ocean. The division into incoming and outgoing signals is not easily identified through net F_E, which is the quantity often measured (Klymak et al. 2011; Kelly et al. 2012).

The cross terms (Fig. 8d) result from random phasing of coherent and incoherent motions. $\langle F_{\text{cross}} \rangle_H$ have similar character and magnitude at each mooring. Because the instantaneous magnitude of $\langle F_{\text{cross}} \rangle_H$ is similar to the coherent and incoherent terms, it is responsible for significant temporal variability of $\langle F_E \rangle_H$. We note that $\langle F_{\text{cross}} \rangle_H$ was persistently negative (onshore) during the period of weakest coherent tides (17–20 August), thus bolstering the instantaneous onshore energy flux at the time when strong onshelf NLIWs were observed.

5. Summary of shelfbreak dynamics

The time-averaged spatial structure of coherent and incoherent contributions are summarized in Fig. 9. At each mooring, F_{coh} is positive at all depths (red shading), and its vertical integral increases with increasing distance offshore from the shelf break. This supports our interpretation that the upper slope is a source of phase-coherent internal tides that primarily radiate their energy offshore. In contrast, F_{inc} is almost exclusively negative (onshore) at all depths, with magnitude decreasing toward shore, consistent with the slope being a sink of energy that originated elsewhere.

Both the vertical structure and magnitude of F_{coh} closely match that modeled assuming barotropic flow

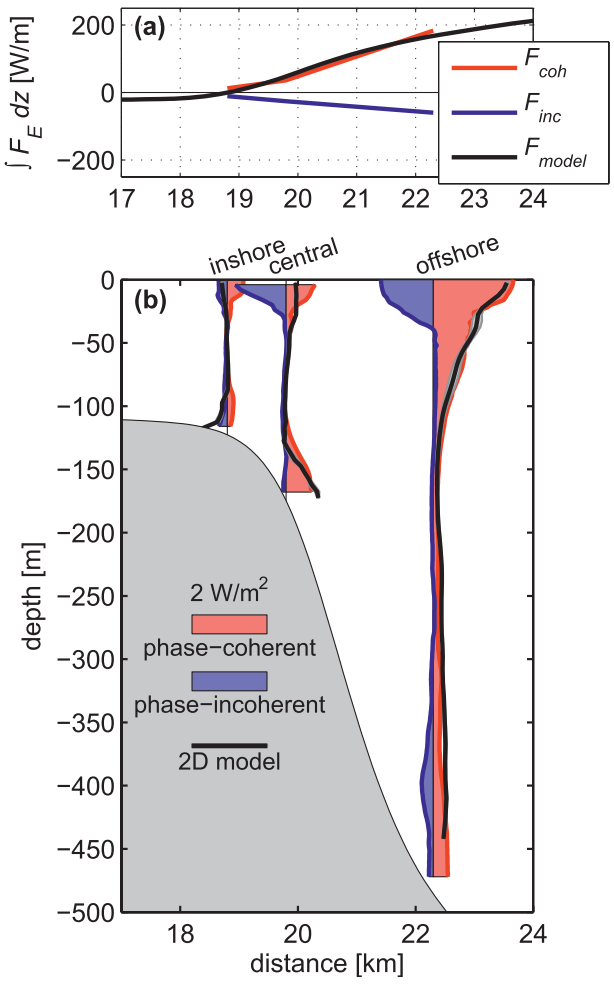

FIG. 9. Time-averaged decomposition of coherent and incoherent motions at the three shelfbreak moorings over the 40-day record. (a) Depth-integrated energy flux in the coherent observations (red), incoherent observations (blue) and barotropically-forced model (black) as a function of distance across the shelf/slope (km). (b) Vertical profiles as above. In these time averages, F_{cross} is small in comparison.

over 2D topography (F_{model}, data from Fig. 5d are replotted in Fig. 9). This quantitative agreement supports the above premise that the locally generated signal is extracted through our harmonic analyses and F_{coh} is mostly predictable. However, over the New Jersey slope, F_{coh} and F_{model} are both directed offshore.

The fact that the coherent contributions match those modeled supports the complementary notion that the incoherent contributions in our data record are associated with dynamics not included in our numerical model. In other words, the coherent/incoherent decomposition has apparently allowed us to discriminate between two types of internal tides in this record: 1) those represented by 2D local generation, and 2) those associated with shoaling tides, three-dimensionality, time-varying mesoscale effects, etc. Because these incoherent motions primarily transmit energy onto the shelf (Fig. 9b; blue), we suggest they control the magnitude and temporal character of onshelf internal tides and NLIWs during this time period.

a. Relationship between tides, internal tides, and NLIWs

The linkages between the slope/shelfbreak dynamics and NLIWs are summarized in Fig. 10. Highlighted are the two periods of strongly differing NLIW activity, during which the structure of F_E and the partitioning between F_{coh} and F_{inc} changed dramatically (Figs. 10a,b). During the spring-tide period (8–16 August), F_{coh} was strongly offshore, while F_{inc} was weak and onshore. During the neap-tide period (16–24 Aug), F_{coh} weakened, as expected since local conversion should scale approximately with u_{bt}^2. At the same time, F_{inc} increased, presumably due to an increase in shoaling internal waves of offshore origin, 3D effects and internal tide refraction, or some combination of these.

Because most of the energy from the coherent internal tide F_{coh} propagates offshore, its connection to the onshelf internal wave energetics is somewhat ambiguous. This is unfortunate since F_{coh} represents the component of the internal tide that is predictable through numerical simulation (i.e., Fig. 5) or theoretical models (i.e., Echeverri and Peacock 2010; St. Laurent et al. 2003). Instead, these observations show that the primary source of energy to the shelf is through the incoherent and cross terms, whose strength is most related to external forcings or 3D effects. In the following we look at the detailed time evolution of local and remote processes to gain insight on how these combine to produce NLIWs on the shelf.

1) LOCAL GENERATION

We consider the perturbation bottom pressure as both a measure of the energy containing internal tide displacements and as a factor that affects local conversion from the barotropic tide through its correlation with u_{bt} [Eq. (1)]. Using the trapezoidal rule, $C = \nabla H \cdot \overline{\mathbf{u}_{\text{bt}} p'}|_{z=-H}$ was integrated across the shelf break for the coherent and incoherent signals from the three cross-shelf moorings.

The coherent bottom pressure (Fig. 10d) increases in amplitude during this observational period, presumably as a result of the increasing stratification (i.e., Fig. 2d). p'_{coh} is completely in-phase with u_{bt}, leading to strong coherent generation C_{coh} that tracks the spring-neap cycle of forcing (Fig. 10e). As a result, the integrated

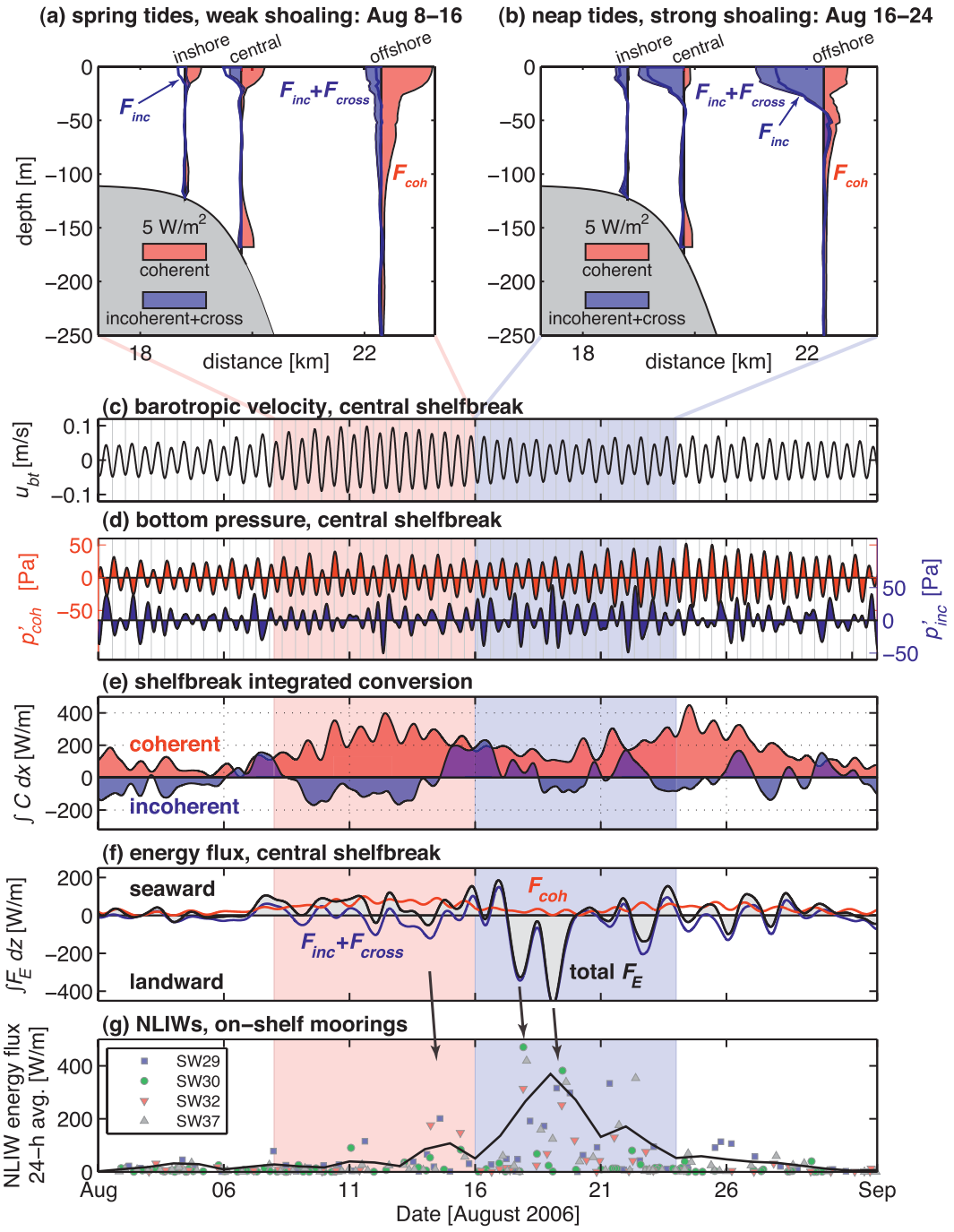

FIG. 10. The shelfbreak structure of $F_{\rm coh}$ (red), $F_{\rm inc} + F_{\rm cross}$ (blue), and $F_{\rm inc}$ (solid dark blue line) during the two contrasting periods: (a) spring tides and weak shoaling, 8–16 Aug; and (b) neap tides and strong shoaling, 16–24 Aug. Shown for perspective are time series of (c) barotropic velocity $u_{\rm bt}$, (d) baroclinic bottom pressure $p'_{\rm coh}$ and $p'_{\rm inc}$, (e) coherent and incoherent conversion, integrated across the shelf break (from inshore to offshore mooring) using the trapezoidal rule, (f) components of the energy flux at the central mooring, and (g) the 24-h average energy flux in the onshelf NLIWs some 20–40 km inshore.

coherent conversion across the shelf break can account for the energy flux leaving the slope past the offshore mooring (i.e., the magnitude and structure of $\int F_{\rm coh}\, dz$ and $\int C_{\rm coh}\, dx$ in Figs. 7c and 10e are very similar).

In contrast, $p'_{\rm inc}$ and $u_{\rm bt}$ are not phase locked (Figs. 10c, d), resulting in variable local conversion $C_{\rm inc} = \nabla H \cdot \overline{\mathbf{u}_{\rm bt} p'_{\rm inc}}|_{z=-H}$ that changes sign on 1–5-day intervals depending on how $u_{\rm bt}$ and $p'_{\rm inc}$ are phased. Thus, there

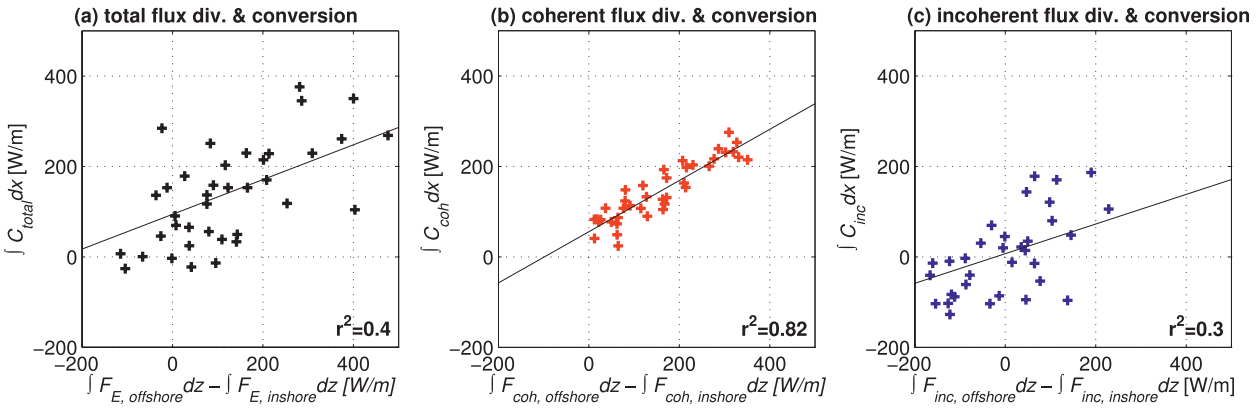

FIG. 11. Relationship between shelfbreak-integrated conversion and energy flux divergence across the shelf break for (a) the total signal, (b) the coherent contribution, and (c) the incoherent contribution.

are periods when the shoaling internal tide either enhances or reduces the local conversion (see Kelly and Nash 2010, for a complete description), but the time-mean contribution C_{inc} is close to zero. While most of the conversion identified in Fig. 10e is coherent (from the local barotropic tide) and anticipated to radiate energy offshore (Fig. 5), periods of incoherent conversion play a role in modulating the shelfbreak flux divergence on shorter time scales.

Scatterplots of $\int C\,dx$ versus 2D flux divergence across the shelf break were computed for the total, coherent, and incoherent signals in Fig. 11. Of the three signals, the coherent conversion rate and flux divergence are most strongly related ($r^2 = 0.8$), which provides some evidence that local generation may be predicted from 2D considerations at this location. On the other hand, the incoherent conversion and flux divergence show a weak relationship ($r^2 = 0.3$). Since we have neglected along-slope gradients in computing divergences, it is possible that the disagreement in Fig. 11c may result from 3D scattering of the shoaling waves. It is also possible that direct dissipation of shoaling tides contributes to the weak correlation, as this would manifest as a flux convergence without requiring $\int C\,dx < 0$. The convergence in ($F_{\text{inc}} + F_{\text{cross}}$) between central and inshore mooring that occurred during the period of strong shoaling (e.g., Fig. 10b) is consistent with dissipation of an incoming tide near the shelf break.

2) SHOALING TIDES

The strongest incoherent pressure perturbation (p'_{inc}) occurred during the 16–24 August period (Fig. 10d), presumably the result of shoaling internal tides as represented through F_{inc} (Fig. 10b). The importance of these shoaling tides is highlighted in the time domain in Fig. 10f, which shows how the incoherent and cross contributions $F_{\text{inc}} + F_{\text{cross}}$ are associated with landward (negative) energy transport at the central shelfbreak mooring.

Figure 10f illustrates how F_{coh} has negligible contribution to the total F_E at the central shelf break during the 17–20 August period, which is controlled entirely by the contributions from F_{inc} and F_{cross}. NLIW energy F_E^* (Fig. 10g) mimics the shelfbreak patterns of F_E. This relationship is quantified in Fig. 12, which shows a strong correlation ($r^2 = 0.8$) between F_E^* and the incoherent contributions at the shelf break ($F_{\text{inc}} + F_{\text{cross}}$).

Anecdotally, there appears to be a one-to-one correspondence between internal tide pulses at the shelfbreak and NLIW occurrence on the shelf. For example, the strongest onshore pulses of incoherent internal tide energy flux occurred on 17–18 and 19–20 August, producing bursts of F_{inc} exceeding 300 W m^{-1}. 8–16 h later, the strongest NLIWs were detected at the onshelf moorings and tracked by shipboard surveys (Shroyer et al. 2010a), some 20–40 km inshore of the shelf break. This time delay is consistent with the observed NLIW propagation speeds of $c \approx 0.7$ m s^{-1} and the energy levels are similar (Shroyer et al. 2011). It is thus strongly suggestive that the strongest observed onshelf NLIWs have evolved from the shoaling, incoherent internal tide of nonlocal origin.

An additional finding from Shroyer et al. (2011) is that many of the largest NLIWs appeared with a high degree of regularity during the 17–23 August period. For example, Fig. 8 of Shroyer et al. (2011) shows that the three largest named NLIW packets (Rosey, Sonny, and Tonya) arrived at the same phase of the tide on 17, 18 and 20 August, as did several other unnamed packets during that period. The occurrence of phase-locked NLIWs would appear to be at odds with the picture that NLIWs evolve from a shoaling, incoherent internal tide. However, a closer examination of the oscillations of u'_{coh} and u'_{inc} and p'_{coh} and p'_{inc} (not shown), reveal that

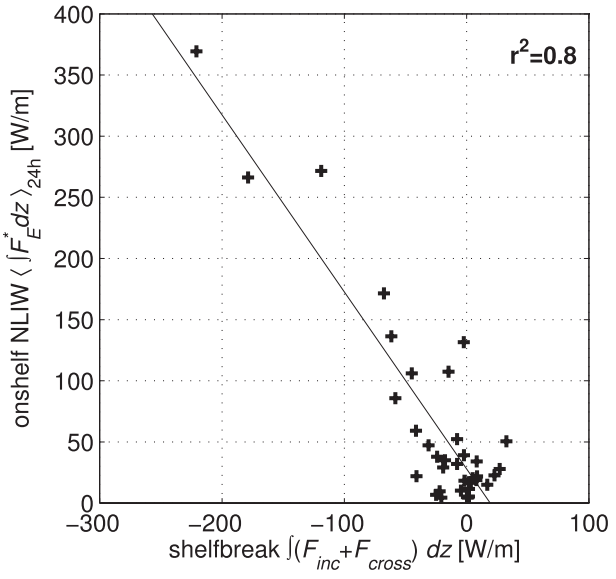

FIG. 12. Relationship between the depth-integrated NLIW energy flux on the shelf ($\langle \int F_E^* \, dz \rangle_{24h}$; from Fig. 10g) and the incoherent contributions to the shelfbreak energy flux at the central shelf break ($\int (F_{inc} + F_{cross}) \, dz$; from Fig. 10f).

these maintain constant phase over periods long enough to contribute to a degree of regularity. As a result, the coherent and incoherent signals added constructively during the period of semiregular NLIW arrivals, so that the onshore velocity pulses were enhanced by the interference and formed at roughly the same phase of the M_2 tide (Fig. 13 of Shroyer et al. 2011). These arguments parallel some of the reasoning of Shroyer et al. (2011) for the interference between M_2 and near-f signals. However a fundamental difference is that M_2 and f go in and out of phase on time scales of O(hours), whereas the coherent and incoherent signals maintain phase coherence for O(days).

b. NLIW and internal tide predictability

By decomposing u' and p' into its coherent and incoherent parts, we have shown that coherent motions at the shelfbreak are consistent with that of a locally generated internal tide. Quantitative agreement between observed and numerically modeled energy fluxes support this assertion (i.e., F_{coh} in Fig. 9). At the same time, incoherent motions are consistent with the shoaling of a remotely generated internal tide. While a large fraction of the incoherent signal is dissipated on the slope, a significant fraction may be intermittently transmitted onto the shallow shelf (i.e., F_{inc} in Fig. 8).

Because the total energy flux F_E is the sum of coherent, incoherent and cross terms [Eq. (9)], F_E is not related to the barotropic shelfbreak forcing in a simple way. This is illustrated in Fig. 13a, which shows how daily-averaged $\int F_E \, dz$ at the central shelfbreak mooring has a spread of more than 100 W m^{-1} and can have either sign (onshore or offshore) for similar values of barotropic forcing, as represented by $N^2 u_{bt}^2$. As a result, $r^2 = 0.05$ for a linear fit. Instead, we find that only the coherent contribution is strongly correlated with $N^2 u_{bt}^2$ yielding $r^2 = 0.54$, as shown in Fig. 13b. However, the coherent tide radiates most of its energy offshore, a result consistent with our numerical simulations. From a 2D perspective, it thus appears that the most predictable part of the internal tide has little consequence to the onshelf internal tide or its NLIWs.

6. Conclusions

Just as the superposition of multiple waves in a broadband surface gravity wavefield produces *sets* of large-amplitude waves in an incoming swell (Longuet-Higgins 1984), the interference of waves transiting the open ocean (Rainville and Pinkel 2006) produces groupiness in the internal tide (van Haren 2004). Such intermittent internal tides are incoherent by nature, meaning that they vary in both phase and/or amplitude from one astronomical tidal cycle to another. With sufficiently long time series, coherent and incoherent motions can be separated.

To explain why the largest internal tides and NLIWs occurred during the period of weakest barotropic tidal forcing (neap), we have performed harmonic analyses to decompose the wavefield into its coherent and incoherent motions. An analysis of the energy flux finds that the observed coherent motions produce offshore radiation of energy, consistent with those simulated using a 2D nonhydrostatic model forced by barotropic tides over topography (Fig. 5).

In contrast, incoherent motions at the shelf break are associated with the onshore transport of energy. While we have not attempted to identify the source of F_{inc}, there are two likely candidates.

(i) First, F_{inc} may be the ultimate fate of the open-ocean internal tide "swell" (Ray and Cartwright 2001; Alford 2003). These distantly generated motions redistribute barotropic energy globally through internal waves and mixing but remain largely indeterministic even with global internal tide models (i.e., Arbic et al. 2010; Simmons et al. 2004). Continental slopes and shelves represent locations where a significant fraction of baroclinic energy may be dissipated (Nash et al. 2004) since internal tides are able to propagate great distances through the deep ocean waveguide (Alford et al. 2007). These are incoherent by nature, except very near large-amplitude topography.

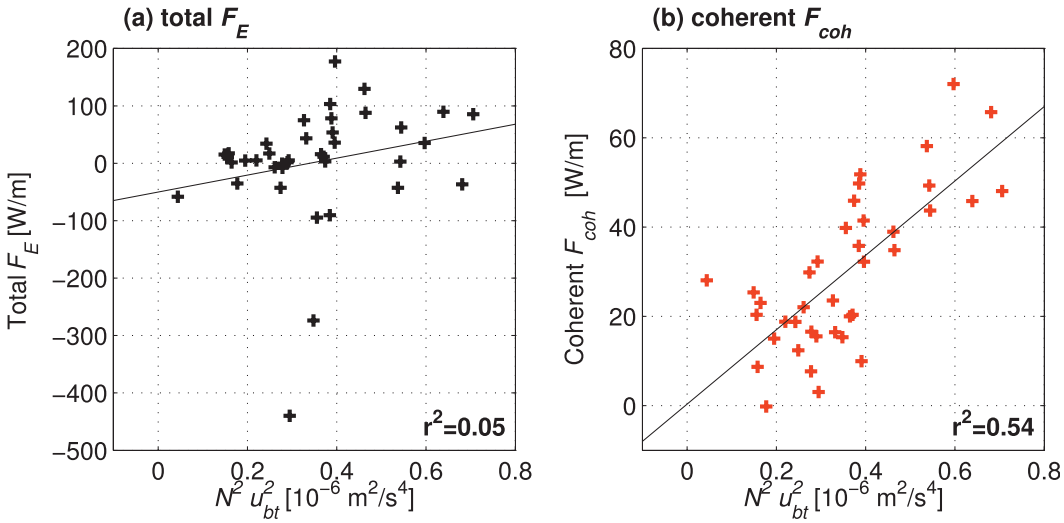

FIG. 13. Relationship between energy flux at the central shelfbreak mooring (SW42) and local forcing, as represented by $N^2 u_{bt}^2$. The total flux is uncorrelated with local forcing. The coherent flux is correlated to local forcing.

(ii) Second, F_{inc} may represent energy generated by phase- or amplitude-modulated processes at or near the New Jersey slope. Such incoherence can arise during local barotropic to baroclinic conversion that is temporally or spatially variable because of the mesoscale. Alternatively, if locally generated internal tides refract back toward the shelf break (as suggested on the Portuguese shelf by Sherwin et al. 2002), then any phase modulation of those waves by the mesoscale will produce incoherence at this site. Moreover, three-dimensional interference can result in chaotic resonances because of interactions between multiple generation sites (Kelly and Nash 2010). Since the New Jersey slope is incised with numerous corrugations and canyons, such 3D variability and interactions are possible.

Our analyses are unable to discern between the above two contributions.

While local generation at the shelf break is dominated by coherent motions, the total energy flux is strongly influenced by incoherent motions, which give rise to onshelf energy transport through the combination of F_{inc} and F_{cross}. At the New Jersey slope, these are of similar amplitudes to F_{coh} (Fig. 9), so that the net cross-shelf, depth-integrated energy flux is zero at some location near the shelf break. This highlights how the net energy flux can be misleading in regions where multiple signals propagate in different directions (Klymak et al. 2011); diagnosing kinetic and available potential energy represent a complementary means of assessing the energetics in regions of strong generation (Nash et al. 2006). In the analysis here, we have been fortunate to have 1) a long enough time series to decompose the coherent and incoherent motions, and 2) this separation yield some insight as to the source of each contribution. At other locations (e.g., on the Oregon slope, Kelly et al. 2012) a similar decomposition may not be effective at partitioning different energy sources.

Despite time-average F_{coh} and F_{inc} being similar in magnitude, at any instant in time the energy transport by phase-incoherent motions and their associated cross terms can exceed those in coherent motions by a factor of 10 or more (Fig. 10f). As a result, periods of strong onshelf internal tides and the degree of nonlinearity are controlled by the incoherent signal that may originate outside of our study site. This finding appears to be a somewhat universal feature of the coastal ocean: an assessment of velocity records from 16 locations around the world (Nash et al. 2012) indicates that the internal-tide variance on most continental shelves is predominantly incoherent on times scales longer than O(1 week).

Although it may take on various forms (e.g., nonlinear internal waves, bores, undular bores, etc.) the nonlinear portion of the internal tide is often a dominant contributor to shelf motions and dynamics. The strong velocity and shear associated with these features has been linked to increased mixing (Moum et al. 2003), suspension of sediment (Bogucki et al. 1997), and transport of mass (Shroyer et al. 2010b) and larvae (Shanks 1983; Pineda 1991). Engineering applications, such as disposal of wastewater and offshore drilling, can be impacted as well, making predictability a desirable trait. The implications of this study, which suggest that the majority of the on-shelf internal tide is related to an incoherent

internal tide, are therefore profound yet discouraging, since the signals of interest may originate 100s or 1000s of kilometers from the site of interest.

Acknowledgments. The authors thank Jim Lynch and Jim Irish for their leadership in the SW06 field program. The measurements would not have been possible without the skilled technical support from John Kemp, Ray Kreth, Mike Neely-Brown, Alexander Perlin, Jim Ryder, James Dunn, Arthur Newhall, Risk Trask, and Neil McPhee. We also thank the captain and crew of R/V *Oceanus* and *Knorr*, and the constructive comments of several anonymous reviewers. This research was supported by ONR Grants N00014-05-1-0271, N00014-08-1-0991, N00014-04-1-0146, and N00014-11-1-0194.

APPENDIX

Calculation of E_a and F_E

The calculation of E_a has been the subject of much discussion because the definition of the reference density $\rho_o(z)$ corresponding to the background potential energy state can significantly alter the computed E_a. Following Shepherd (1993), Scotti et al. (2006), Lamb (2007), and Lamb and Nguyen (2009), we define E_a as

$$E_a = g \int_{\rho_o(z)}^{\rho} z - z^*(s)\, ds, \tag{A1}$$

where ρ is the wave-perturbed density, and $z^*(s)$ is the vertical location of the reference density s such that $\rho_o[z^*(s)] = s$.

Wave pressure (Moum and Smyth 2006; Moum and Nash 2008) is computed as

$$p' = p'_h + p'_\eta + p'_{\rm nh}, \tag{A2}$$

where $p'_h(z) = g \int_z^0 \rho'\, dz'$ is the hydrostatic pressure associated with the wave-induced density $\rho'(z) = \rho(z) - \rho_o(z)$, $p'_\eta = \rho_o g \eta$ is the external hydrostatic pressure associated with the wave-induced surface displacement η, and $p'_{\rm nh} = \rho_o \int_z^0 Dw/Dt\, dz'$ is the nonhydrostatic pressure. As in Moum and Nash (2008), we assume a wave of permanent form moving at speed c to estimate the advective term in D/Dt (i.e., $\partial/\partial x \approx c^{-1}\partial/\partial t$). Finally, the surface displacement may be computed as $\eta = -(1/g) \int_{-\infty}^{x} Du'/Dt\, dx'$ if near-surface velocity is available. Alternatively, the baroclinicity condition $\int_{-H}^{0} p'\, dz = 0$ (Kunze et al. 2002) can be applied to determine η. In practice, both give similar estimates of η.

In the absence of sufficient in situ CTD data that resolves wave displacement, ρ' and p' can be determined from well-resolved ADCP data (Moum and Smyth 2006). For a wave that propagates at speed c without substantial change of form, the streamfunction $\psi(x - ct, z)$ can be calculated from either vertical integration of u' or horizontal integration of w'. Following Moum and Smyth (2006) Eqs. (6.1)–(6.5), we compute ψ both ways and average. Density is then mapped onto streamlines and pressure computed from regridded fields, provided that an upstream or background reference density profile can be identified. Fortunately, extensive CTD data were obtained during shipboard wave-tracking experiments that captured both the background ρ_o and perturbation ρ' across the entire shelf on a fairly regular basis (Shroyer et al. 2010a, 2011) with sub-10 cm vertical resolution. Density data from glider transects (Castelao et al. 2008) were available on weekly time scales for periods outside the intensive wave-tracking period (1–25 August).

The above procedure is particularly useful when a strong pycnocline exists and C/T sensor spacing is $O(10\ \text{m})$ or greater. In such cases, a wave can displace fluid 10 m without appreciable changes in measured density or pressure, if the pycnocline falls just below the upper sensor. If fluid is displaced 20 m (for example), measured density may exhibit just a single step-change at peak vertical displacement, producing significant error in p' and E_a. Computing density from ADCP-derived streamlines resolves this by producing smooth profiles of ρ' and p' that are consistent with discrete sensors when available.

REFERENCES

Alford, M. H., 2003: Energy available for ocean mixing redistributed by long-range propagation of internal waves. *Nature,* **423,** 159–162.

——, J. A. MacKinnon, Z. Zhao, R. Pinkel, J. M. Klymak, and T. Peacock, 2007: Internal waves across the Pacific. *Geophys. Res. Lett.,* **34,** L24601, doi:10.1029/2007GL031566.

Apel, J. R., and Coauthors, 1997: An overview of the 1995 SWARM shallow-water internal wave acoustic scattering experiment. *IEEE J. Oceanic Eng.,* **22,** 465–500.

Arbic, B., A. Wallcraft, and E. Metzger, 2010: Concurrent simulation of the eddying general circulation and tides in a global ocean model. *Ocean Modell.,* **32,** 175–187.

Baines, P. G., 1982: On internal tide generation models. *Deep-Sea Res.,* **29,** 307–338.

Bogucki, D., T. Dickey, and L. G. Redekopp, 1997: Sediment resuspension and mixing by resonantly generated internal solitary waves. *J. Phys. Oceanogr.,* **27,** 1181–1196.

Brickman, D., and J. Loder, 1993: Energetics of the internal tide on northern Georges Bank. *J. Phys. Oceanogr.,* **23,** 409–424.

Buijsman, M., Y. Uchiyama, J. McWilliams, and C. Hill-Lindsay, 2012: Modeling semidiurnal internal tide variability in the Southern California Bight. *J. Phys. Oceanogr.,* **42,** 62–77.

Carter, G., and Coauthors, 2008: Energetics of M2 barotropic-to-baroclinic tidal conversion at the Hawaiian Islands. *J. Phys. Oceanogr.,* **38,** 2205–2223.

Castelao, R., O. Schofield, S. Glenn, R. Chant, and J. Kohut, 2008: Cross-shelf transport of freshwater on the New Jersey shelf. *J. Geophys. Res.,* **113,** C07017, doi:10.1029/2007JC004241.

Chavanne, C., P. Flament, D. Luther, and K.-W. Gurgel, 2010: The surface expression of semidiurnal internal tides near a strong source at Hawaii. Part II: Interactions with mesoscale currents. *J. Phys. Oceanogr.,* **40,** 1180–1200.

Colosi, J. A., and W. Munk, 2006: Tales of the venerable Honolulu tide gauge. *J. Phys. Oceanogr.,* **36,** 967–996.

——, R. C. Beardsley, J. F. Lynch, G. Gawarkiewicz, C. Chiu, and A. Scotti, 2001: Observations of nonlinear internal waves on the outer New England continental shelf during the summer Shelfbreak Primer study. *J. Geophys. Res.,* **106** (C5), 9587–9601.

Duda, T., and L. Rainville, 2008: Diurnal and semidiurnal internal tide energy flux at a continental slope in the South China Sea. *J. Geophys. Res.,* **113,** C03025, doi:10.1029/2007JC004418.

Dushaw, B., P. Worcester, and M. Dzieciuch, 2011: On the predictability of mode-1 internal tides. *Deep-Sea Res. I,* **58,** 677–698.

Echeverri, P., and T. Peacock, 2010: Internal tide generation by arbitrary two-dimensional topography. *J. Fluid Mech.,* **659,** 247–266.

Egbert, G. D., 1997: Tidal inversion: Interpolation and inference. *Prog. Oceanogr.,* **40** (1–4), 53–80.

Gerkema, T., F. Lam, and L. Maas, 2004: Internal tides in the Bay of Biscay: Conversion rates and seasonal effects. *Deep-Sea Res. II,* **51,** 2995–3008.

Guo, C., X. Chen, V. Vlasenko, and N. Stashchuk, 2011: Numerical investigation of internal solitary waves from the Luzon Strait: Generation process, mechanism and three-dimensional effects. *Ocean Modell.,* **38** (3–4), 203–216.

Henyey, F. S., and A. Hoering, 1997: Energetics of borelike internal waves. *J. Geophys. Res.,* **102** (C2), 3323–3330.

Hosegood, P., and H. van Haren, 2006: Sub-inertial modulation of semi-diurnal currents over the continental slope in the Faeroe-Shetland Channel. *Deep-Sea Res. I,* **53,** 627–655.

Inall, M., T. Rippeth, and T. Sherwin, 2000: Impact of nonlinear waves on the dissipation of internal tidal energy at a shelf break. *J. Geophys. Res.,* **105,** 8687–8705.

Kelly, S. M., and J. D. Nash, 2010: Internal-tide generation and destruction by shoaling internal tides. *Geophys. Res. Lett.,* **37,** L23611, doi:10.1029/2010GL045598.

——, ——, and E. Kunze, 2010: Internal-tide energy over topography. *J. Geophys. Res.,* **115,** C06014, doi:10.1029/2010GL045598.

——, ——, K. Martini, M. Alford, and E. Kunze, 2012: The cascade of tidal energy from low to high modes on a continental slope. *J. Phys. Oceanogr.,* **42,** 1217–1232.

Klymak, J., S. Legg, and R. Pinkel, 2010a: High-mode stationary waves in stratified flow over large obstacles. *J. Fluid Mech.,* **644,** 321–336.

——, ——, and ——, 2010b: A simple parameterization of turbulent tidal mixing near supercritical topography. *J. Phys. Oceanogr.,* **40,** 2059–2074.

——, M. Alford, R. Pinkel, R. Lien, Y. Yang, and T. Tang, 2011: The breaking and scattering of the internal tide on a continental slope. *J. Phys. Oceanogr.,* **41,** 926–945.

Kunze, E. L., L. K. Rosenfeld, G. S. Carter, and M. C. Gregg, 2002: Internal waves in Monterey Submarine Canyon. *J. Phys. Oceanogr.,* **32,** 1890–1913.

Kurapov, A., G. Egbert, J. Allen, R. Miller, S. Erofeeva, and P. Kosro, 2003: The M2 internal tide off Oregon: Inferences from data assimilation. *J. Phys. Oceanogr.,* **33,** 1733–1757.

Lamb, K. G., 1994: Numerical experiments of internal wave generation by strong tidal flow across a finite amplitude bank edge. *J. Geophys. Res.,* **99** (C1), 843–864.

——, 2007: Energy and pseudoenergy flux in the internal wave field generated by tidal flow over topography. *Cont. Shelf Res.,* **27,** 1208–1232.

——, and V. T. Nguyen, 2009: Calculating energy flux in internal solitary waves with an application to reflectance. *J. Phys. Oceanogr.,* **39,** 559–580.

Lee, C. M., E. Kunze, T. B. Sanford, J. D. Nash, M. A. Merrifield, and P. E. Holloway, 2006: Internal tides and turbulence along the 3000-m isobath of the Hawaiian Ridge. *J. Phys. Oceanogr.,* **36,** 1165–1183.

Lerczak, J. A., C. D. Winant, and M. C. Hendershott, 2003: Observations of the semidiurnal internal tide on the southern California slope and shelf. *J. Geophys. Res.,* **108,** 3068, doi:10.1029/2001JC001128.

Li, Q., and D. Farmer, 2011: The generation and evolution of nonlinear internal waves in the deep basin of the South China Sea. *J. Phys. Oceanogr.,* **41,** 1345–1363.

Longuet-Higgins, M., 1984: Statistical properties of wave groups in a random sea state. *Philos. Trans. Roy. Soc. London,* **A312,** 219–250

MacKinnon, J. A., and M. C. Gregg, 2003: Shear and baroclinic energy flux on the summer New England shelf. *J. Phys. Oceanogr.,* **33,** 1462–1475.

Marshall, J., A. Adcroft, C. Hill, L. Perelman, and C. Heisey, 1997: A finite-volume, incompressible Navier Stokes model for studies of the ocean on parallel computers. *J. Geophys. Res.,* **102,** 5753–5766.

Moum, J. N., and W. Smyth, 2006: The pressure disturbance of a nonlinear internal wave train. *J. Fluid Mech.,* **558,** 153–177.

——, and J. D. Nash, 2008: Seafloor pressure measurements of nonlinear internal waves. *J. Phys. Oceanogr.,* **38,** 481–491.

——, D. M. Farmer, W. D. Smyth, L. Armi, and S. Vagle, 2003: Structure and generation of turbulence at interfaces strained by internal solitary waves propagating shoreward over the continental shelf. *J. Phys. Oceanogr.,* **33,** 2093–2112.

——, J. M. Klymak, J. D. Nash, A. Perlin, and W. D. Smyth, 2007: Energy transport by nonlinear internal waves. *J. Phys. Oceanogr.,* **37,** 1968–1988.

Nash, J. D., E. Kunze, J. M. Toole, and R. W. Schmitt, 2004: Internal tide reflection and turbulent mixing on the continental slope. *J. Phys. Oceanogr.,* **34,** 1117–1134.

——, M. H. Alford, and E. Kunze, 2005: Estimating internal wave energy fluxes in the ocean. *J. Atmos. Oceanic Technol.,* **22,** 1551–1570.

——, E. Kunze, C. M. Lee, and T. B. Sanford, 2006: Structure of the baroclinic tide generated at Kaena Ridge, Hawaii. *J. Phys. Oceanogr.,* **36,** 1123–1135.

——, E. L. Shroyer, S. M. Kelly, M. E. Inall, T. F. Duda, M. D. Levine, N. L. Jones, and R. C. Musgrave, 2012: Are any coastal internal tides predictable? *Oceanography (Wash. D.C.),* **25,** 80–95.

Newhall, A., and Coauthors, 2007: Acoustic and oceanographic observations and configuration information for the WHOI moorings from the SW06 experiment. Woods Hole Oceanographic Institution Tech. Rep. WHOI-2007-04, 116 pp.

Osborne, J. J., A. L. Kurapov, G. D. Egbert, and P. M. Kosro, 2011: Spatial and temporal variability of the M2 internal tide generation and propagation on the Oregon shelf. *J. Phys. Oceanogr.,* **41,** 2037–2062.

Pineda, J., 1991: Predictable upwelling and the shoreward transport of planktonic larvae by internal tidal bores. *Science,* **253,** 548–551.

Pingree, R. D., and A. L. New, 1991: Abyssal penetration and bottom reflection of internal tide energy into the Bay of Biscay. *J. Phys. Oceanogr.,* **21,** 28–39.

Rainville, L., and R. Pinkel, 2006: Propogation of low-mode internal waves through the ocean. *J. Phys. Oceanogr.,* **36,** 1220–1236.

——, T. Johnston, G. Carter, M. Merrifield, R. Pinkel, P. Worcester, and B. Dushaw, 2010: Interference pattern and propagation of the M2 internal tide south of the Hawaiian Ridge. *J. Phys. Oceanogr.,* **40,** 311–325.

Ramp, S., Y. Yang, and F. Bahr, 2010: Characterizing the nonlinear internal wave climate in the northeastern South China Sea. *Nonlinear Processes Geophys.,* **17,** 481–498.

Rattray, M., 1960: On the coastal generation of internal tides. *Tellus,* **12,** 54–62, doi:10.1111/j.2153-3490.1960.tb01283.x.

Ray, R., and D. Cartwright, 2001: Estimates of internal tide energy fluxes from TOPEX/Poseidon altimetry: Central North Pacific. *Geophys. Res. Lett.,* **28,** 1259–1262.

Savidge, D., C. Edwards, and M. Santana, 2007: Baroclinic effects and tides on the Cape Hatteras continental shelf. *J. Geophys. Res.,* **112,** C09016, doi:10.1029/2006JC003832.

Scotti, A., R. Beardsley, and B. Butman, 2006: On the interpretation of energy and energy fluxes of nonlinear internal waves: An example from Massachusetts Bay. *J. Fluid Mech.,* **561,** 103–112.

——, ——, ——, and J. Pineda, 2008: Shoaling of nonlinear internal waves in Massachusetts Bay. *J. Geophys. Res.,* **113,** C08031, doi:10.1029/2008JC004726.

Shanks, A., 1983: Surface slicks associated with tidally forced internal waves may transport pelagic larvae of benthic invertebrates and fishes shoreward. *Mar. Ecol. Prog. Ser. Oldendorf,* **13,** 311–315.

Shepherd, T., 1993: A unified theory of available potential energy. *Atmos.–Ocean,* **31,** 1–1.

Sherwin, T., V. Vlasenko, N. Stashchuk, D. Jeans, and B. Jones, 2002: Along-slope generation as an explanation for some unusually large internal tides. *Deep-Sea Res. I,* **49,** 1787–1799.

Shroyer, E., J. Moum, and J. Nash, 2010a: Energy transformations and dissipation of nonlinear internal waves over New Jersey's continental shelf. *Nonlinear Processes Geophys.,* **17,** 345–360.

——, ——, and ——, 2010b: Vertical heat flux and lateral mass transport in nonlinear internal waves. *Geophys. Res. Lett.,* **37,** L08601, doi:10.1029/2010GL042715.

——, ——, and ——, 2011: Nonlinear internal waves over New Jersey's continental shelf. *J. Geophys. Res.,* **116,** C03022, doi:10.1029/2010JC006332.

Simmons, H., R. Hallberg, and B. Arbic, 2004: Internal wave generation in a global baroclinic tide model. *Deep-Sea Res.,* **51,** 3043–3068.

Small, J., Z. Hallock, G. Pavey, and J. Scott, 1999: Observations of large amplitude internal waves at the Malin Shelf edge during SESAME 1995. *Cont. Shelf Res.,* **19,** 1389–1436.

St. Laurent, L., S. Stringer, C. Garrett, and D. Perrault-Joncas, 2003: The generation of internal tides at abrupt topography. *Deep-Sea Res.,* **50,** 987–1003.

Tang, D., and Coauthors, 2007: Shallow Water'06: A joint acoustic propagation/nonlinear internal wave physics experiment. *Oceanography (Wash. D.C.),* **20,** 156–167.

van Haren, H., 2004: Incoherent internal tidal currents in the deep ocean. *Ocean Dyn.,* **54,** 66–76.

Zilberman, N. V., M. A. Merrifield, G. S. Carter, D. S. Luther, M. D. Levine, and T. J. Boyd, 2011: Incoherent nature of M2 internal tides at the Hawaiian Ridge. *J. Phys. Oceanogr.,* **41,** 2021–2036.